2D radiation-hydrodynamics modeling of laser-plasma targets for ion stopping measurements☆

An. Tauschwitz[a,b,*], M. Basko[a,c], A. Frank[d], V. Novikov[f], A. Grushin[f], A. Blazevic[e], M. Roth[d], J.A. Maruhn[a,b]

[a]*ExtreMe Matter Institute EMMI, GSI Helmholtzzentrum für Schwerionenforschung, Germany*
[b]*University of Frankfurt am Main, Germany*
[c]*Institute of Theoretical and Experimental Physics, Moscow, Russia*
[d]*Technische Universität Darmstadt, Germany*
[e]*GSI Helmholtzzentrum für Schwerionenforschung, Germany*
[f]*Keldysh Institute of Applied Mathematics, Moscow, Russia*

Abstract

Two-dimensional radiation hydrodynamics calculations were performed to analyze how a homogeneous plasma layer for ion-stopping measurements can be created by direct laser irradiation of thin carbon foils. At the initial stage, the assumed (so as to imitate the discussed experimental conditions) strongly non-uniform intensity distribution in the laser spot leads to the formation of relatively dense and cold clumps in the plasma. However, it is shown that after several nanoseconds the clumpy structure dissipates predominantly due to the energy transport by thermal radiation. Laser irradiation schemes with the fundamental and doubled frequency light, as well as one- and two-sided heating of the target foil are analyzed and compared. We find that the two-sided irradiation with the doubled laser frequency creates a fully ionized plasma layer and allows to reduce the plasma column-density variations to a level of $\lesssim 1\%$.

Keywords: radiation hydrodynamics, laser-produced plasma, ion stopping measurement
PACS:

1. Introduction

Although many high-accuracy measurements of heavy-ion stopping in matter at normal conditions have been performed [1, 2], the experimental data on ion stopping in plasmas is rather scarce. The knowledge of ion-beam stopping in this regime is of crucial importance for the indirect drive scenario of heavy ion fusion [3] and for the ion-driven fast ignition concept [4, 5]. In the last two decades a number of experiments on measuring the ion energy losses in laser-generated plasmas were performed [6, 7, 8, 9]. The main difficulty in such experiments has always been creation of a uniform plasma layer with a lifetime that would be sufficiently long for the measurements.

For ion-stopping measurements in cold matter usually planar foil targets are used. A straightforward way to create a planar layer of plasma would be to heat up a cold foil by direct laser irradiation. The main drawback of this scheme is inevitable spatial non-uniformities of laser-heated plasma targets. In this work we investigate how a sufficiently uniform plasma layer can be created by direct irradiation of a carbon foil with a nanosecond laser pulse at an average intensity of 5×10^{11} W/cm^2, which exhibits strong fluctuations across the focal spot. Our study is directly related to the corresponding experiments performed at the GSI Helmholtzzentrum für Schwerionenforschung, Darmstadt [9].

To obtain reliable experimental data on the energy loss of fast ions in a plasma, it is advantageous to create a plasma slab with a constant degree of ionization, z_{ion}, where every beam ion encounters the same number of free, $\langle n_e x \rangle = \int n_e \, dx$, and bound electrons along its trajectory. The presented calculations demonstrate how this can be achieved in practice with realistic laser beam parameters. Even when the laser intensity varies by almost 100% over

☆Published in High Energy Density Physics **9** (2013) 158-166
*Corresponding author. Address: Institut für Theoretische Physik, Goethe-Universität Frankfurt am Main, Max-von-Laue–Str. 1, 60438 Frankfurt am Main, Germany. Tel.: +49 (0)69 798-47870.
Email address: an.tauschwitz@gsi.de (An. Tauschwitz)

the focal spot, the combination of frequency doubling (for Nd:YAG $\lambda_{2\omega} = 0.532\,\mu$m) with the two-sided heating of the target foil turns out to be efficient enough in reducing the amplitude of transverse column density variations down to a level of ±0.5% over the timescale of $\simeq$ 10 ns. We have found that the key role in smoothing out spatial non-uniformities belongs to the energy transport by thermal radiation. The reported calculations proved to be important for correct interpretation of the experimental results on the ion stopping in a carbon plasma obtained recently at GSI [9].

The paper is organized as follows. In section 2 we describe the target configuration and laser beam parameters together with the numerical code used for calculations. Section 3 is devoted to the analysis of the results of simulations for several characteristic cases. Special attention is paid to the role of radiation transport in dissolving spatial non-uniformities of the plasma density and temperature distributions. The conclusions are presented in Sec. 4.

2. Formulation of the problem

2.1. Target configuration

We consider laser irradiation of a planar carbon foil at normal incidence. In Fig. 1 the experimental and the simulated target-beam geometries are shown. The laser and the target parameters are taken from the experiments performed with the nhelix and Phelix lasers at GSI [10, 11]. In the experiment the laser beam of radius $r_{foc} \simeq 1$ mm was quasi axially symmetric. In the simulations, however, we used the Cartesian (x, y) geometry, shown schematically in Fig. 1(b), where nothing depends on z, the laser light propagates along the x-axis, and the focal spot has a shape of a band with a halfwidth r_{foc} along y. Such modification of the simulation geometry provides a major simplification for the radiation transport package in the RALEF-2D code [12], which is still under development and whose (r, z)-mode of transport has not been completed yet.

In the experiments, aimed at a quasi planar target configuration, the irradiated carbon foil had the initial thickness $d = 0.5\,\mu$m about 1000 times smaller than the laser focal spot. In the simulations the initial foil thickness was taken to be $d = 1\,\mu$m (but at half the normal carbon density) in order to improve the quality of the numerical mesh and speed up the simulations. The physical impact of such artificial density reduction on the overall plasma dynamics is insignificant because the foil is initially very thin. In the case of two-sided heating of the foil with two laser beams, the y-axis was treated as the plane of symmetry and only half of the foil was considered.

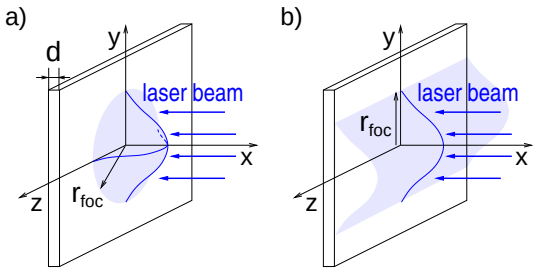

Figure 1: a) Experimental and b) simulated target-beam geometries.

2.2. Laser beam parameters

The nhelix laser at GSI is a Nd:YAG laser with the fundamental frequency (1ω) at the wavelength $\lambda_{1\omega} = 1.064\,\mu$m. For a homogeneous laser spot of radius $r_{foc} \approx 1$ mm the peak irradiation intensity is close to $F_{las} = 5 \times 10^{11}$ W/cm^2. The laser pulse, used in the experiment and the simulations, is 13 ns long ramped with a 3 ns rise and fall intervals. Also, the simulated laser beam was assumed to have no geometrical divergence. Experiments with the Phelix laser were done using essentially the same laser beam parameters.

For the spatial profile of irradiation intensity, where no small-scale non-uniformities were modeled, we have adopted the functional form

$$f(y) = \begin{cases} 1\,, & 0 \le y \le y_{foc}, \\ f_L = \left[1 + (y - y_{foc})^2/\sigma_L^2\right]^{-1}\,, & y_{foc} < y \le y_{foc} + y_L, \\ f_L \cdot f_G = f_L \cdot \exp\left[-\left(y - y_{foc} - y_L\right)^2/\sigma_G^2\right], & y_{foc} + y_L < y, \end{cases} \tag{1}$$

where $y_{foc} = 0.45$ mm, $y_L = 1.3$ mm, $\sigma_L = \sigma_G = 0.15$ mm. A relatively smooth falloff of the laser intensity in the Lorentzian wings was used to avoid the "flip-over" singularities along the Lagrangian plasma-vacuum interface at the periphery of the laser spot. The details of the intensity profile in the wings are insignificant for the physical issues discussed in this paper.

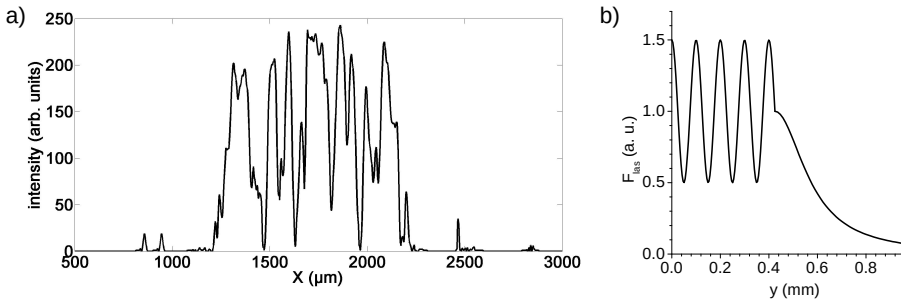

Figure 2: Laser intensity distributions for 1ω light: a) measured across the focal spot, b) assumed in the simulations.

Figure 2a shows a typical lineout of the experimentally measured intensity distribution across the focal spot in the 1ω laser light. The intensity variations have an amplitude of almost 100% on a spatial scale of about 50–100 μm. In the experiments this pattern remained stable in space and time during the entire laser pulse. To model the effect of such non-uniform laser irradiation, we used a periodic function

$$f(y) = 1 + 0.5\cos(2\pi y/l), \quad 0 \le y \le y_{foc}, \tag{2}$$

with $l = 100$ μm over the flat-top part of the spatial profile. The resulting full intensity profile used in the simulations for the 1ω case is shown in Fig 2b. For the 2ω light the random phase plate produces non-uniformities of roughly half the scale length. Hence, in the calculations for the 2ω light the same profile (2) but with $l = 50$ μm was used.

2.3. Radiation hydrodynamics code

The simulations were done with the newly developed 2D radiation hydrodynamics code RALEF-2D [12, 13]. This code is based on the CAVEAT hydrodynamics package [14], which uses a second order Godunov-like scheme on a structural quadrilateral grid and employs the arbitrary Lagrangian-Eulerian technique. Implementation of heat conduction [15] and radiation transport is based on the symmetric semi-implicit method of Ref. [16]. Propagation of thermal radiation and laser beams is treated in three dimensions. The equation of spectral radiation transfer is solved in a quasi-static approximation by a short-characteristic method and using the S_n quadratures for angular discretization. The radiation source function is assumed to be Planckian.

2.4. Equation of state and opacities

The simulations were performed using the equation of state based on the average ion model [17], which accounts for both the thermal and the pressure ionization at high temperatures and/or densities, as well as for realistic properties of materials near normal conditions. Thermal conductivity and spectral opacities were generated by the THERMOS code [18]. In this work we used fully equilibrium (LTE) opacities. Energy transport by thermal radiation was treated with 5 spectral groups delineated by the photon energies

$$h\nu_i = 0,\ 0.02,\ 0.1,\ 0.25,\ 1.0,\ 5.0 \quad \text{[keV]}. \tag{3}$$

The original THERMOS opacities have been averaged over the selected spectral groups with the Planckian weight function. Figure 3 illustrates the spectral dependence of the group absorption coefficients $k_\nu(\rho, T)$ for the selected 5 spectral groups as compared with the original THERMOS spectral data for two pairs of the density and temperature values.

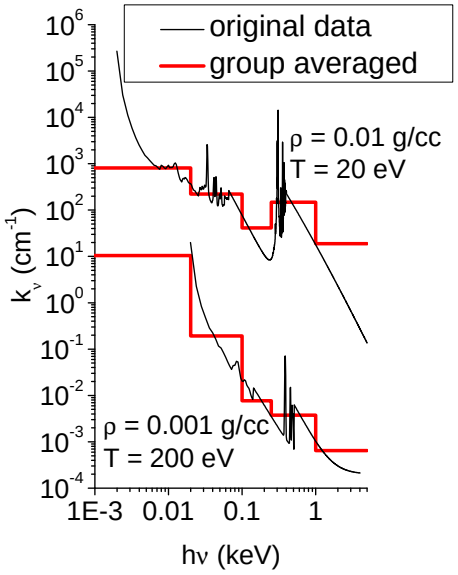

Figure 3: Radiation absorption coefficient k_ν [cm^{-1}] of carbon at $\rho = 0.01$ g/cm^3, T=20 eV and $\rho = 0.001$ g/cm^3, T=200 eV as a function of the photon energy $h\nu$. Thin curve: the original THERMOS data, thick histogram curve: the Planckian average over the selected 5 spectral groups.

For the laser absorption, the analytical Kramers formula for the inverse bremsstrahlung was used. Refraction and reflection of the laser beam were neglected.

2.5. Initial state and boundary conditions

In simulations the initial mass thickness of the carbon foil was fixed at the experimental value $\langle \rho x \rangle = 0.1$ mg/cm^2, but the initial density was chosen to be $\rho_0 = 1$ g/cm^3 — i.e. about a factor 2 below the normal density of carbon. The foil was placed at $x = 0$. The initial pressure was set equal to $p_0 = 5$ kbar, which, at $\rho_0 = 1$ g/cm^3, corresponds to the initial temperature of $T_0 = 0.5$ eV. For the one-sided heating a rectangular region at $0 \le x \le 1\,\mu$m, $0 \le y \le 1.7$ mm with a reflective boundary condition along the x-axis was simulated. For the two-sided heating, one half of the foil was considered with an additional reflective boundary along the y-axis.

To stabilize the simulations, the boundary condition of a fixed external pressure $p_b = 5$ kbar was applied along the remaining physical boundaries. The impact of such artificial external pressure on the plasma dynamics is small and can be judged by the amount of work done by this pressure: at all times it remains below 2% of the energy deposited by the laser.

3. Simulation results

When a thin foil is heated by a relatively broad laser beam at normal incidence, one can distinguish between two types of the density and temperature non-uniformity arising in the created plasma, namely, the longitudinal non-uniformity and the transverse one (with respect to the laser propagation direction). Clearly, a longitudinal non-uniformity develops even when the laser irradiation is perfectly uniform — simply because a hot plasma layer rapidly expands, and because the laser energy is absorbed in a narrow (in terms of the mass thickness) surface layer. The transverse non-uniformity, on the contrary, is typically caused by variation of the laser intensity across the focal

spot and by the hydrodynamic instability. Below we analyze both types under the conditions where the transverse non-uniformity is fully dominated by strong spatial variations of the laser irradiation intensity.

3.1. One-sided foil irradiation with the 1ω light

3.1.1. Uniform laser spot

Here we examine the longitudinal non-uniformity of the irradiated foil. Although this problem can be addressed within a purely one-dimensional (1D) model, two-dimensional results are presented to display the overall large-scale dynamics of the heated foil. Figure 4 shows the 2D temperature distribution by the end of the laser pulse at $t = 10$ ns. It is seen that the rear side of the foil remains relatively cold, which implies a strongly non-uniform profile of the ionization degree along the presumed trajectories of fast ions.

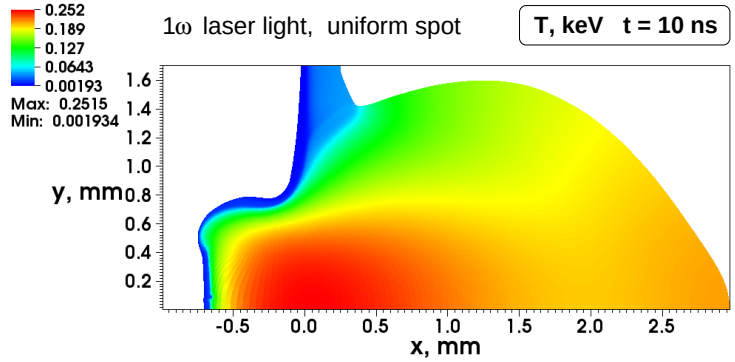

Figure 4: Two-dimensional color-contour plot of matter temperature at $t = 10$ ns for a homogeneous laser spot at 1ω.

Figure 4 reveals a characteristic 2D feature of the overall dynamics of a thin foil irradiated by a broad laser beam. An interesting feature is that the foil ruptures not where the laser intensity is maximum (i.e. at $y = 0$) but rather where the transverse gradient of the laser intensity is maximum (i.e. near $y = 0.5$ mm). This occurs because, as a high ablation pressure at the focal spot pushes forward (i.e. in the negative x-direction) the central part of the foil, the periphery of the irradiated region is stretched, its mass thickness diminishes and, as a consequence, this periphery becomes the first to be burnt through by the laser light.

To analyze the effect of energy transport by thermal radiation on the properties of the created plasma layer, the simulation was also run with the radiation transport turned off. Figure 5 compares the two 1D temperature profiles, plotted as functions of column density along the line $y = 0$ at $t = 5$ ns, as calculated with and without radiation transport. Without radiation transport more mass is ablated by the laser, and the critical surface lies deeper than in the case with radiation. This is caused by the radiative energy loss, which by the end of the laser pulse amounts to some 15% of the deposited laser energy.

A more important consequence of the radiation transport, manifested by Fig. 5, is however a significant amount of preheat by relatively hard x-ray photons, propagating from the hot laser corona, which raise the temperature of the cold rear foil side to $T \simeq 3$–10 eV before the main thermal wave arrives. As a result, a sharp density peak, observed in the case without radiation transport (see Fig. 6), is dramatically broadened (by more than a factor of 10) when the radiant energy exchange is properly accounted for. Clearly, this effect is very important for smoothing out small-scale spatial non-uniformities and, in particular, for suppressing the Rayleigh-Taylor (RT) instability of the accelerated cold layer. Note that the role of the thermal conduction, included in both simulations, turns out to be rather insignificant in this regard.

Earlier or later, the effects of the global 2D plasma expansion must show up in the temporal evolution of the column mass density $\langle \rho x \rangle = \int \rho \, dx$ along the presumed path of the fast ion beam. Figure 7 displays the time dependence of $\langle \rho x \rangle$ calculated along the line $y = 0.15$ mm that would encompass about half of the ion trajectories in a beam of radius $r_b = 0.25$ mm. To conduct clean ion stopping measurements, one would definitely want $\langle \rho x \rangle$ to stay constant. From the data in Fig. 7 one infers that in our case the ion stopping measurements should be performed not later than around $t = 9$ ns, when the plasma column density $\langle \rho x \rangle$ already drops by about 10%. As might be expected, without

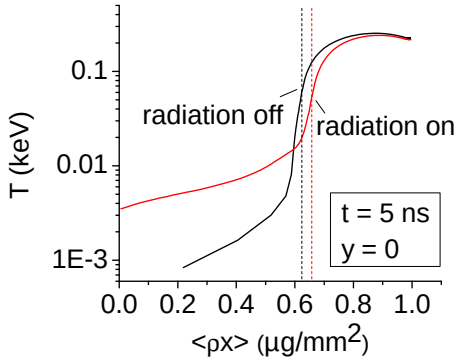

Figure 5: Temperature profiles along $y = 0$ at $t = 5$ ns versus column density as calculated with and without radiation transport. Dashed vertical lines mark the position of the critical surface.

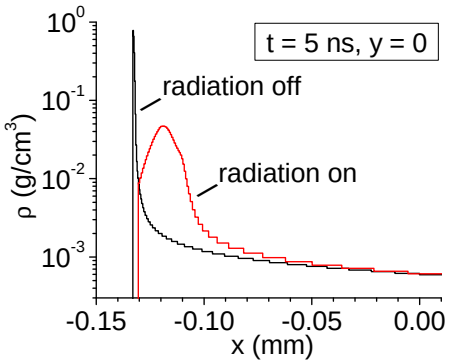

Figure 6: One-dimensional spatial density profiles along the $y = 0$ line at $t = 5$ ns in cases with and without thermal radiation.

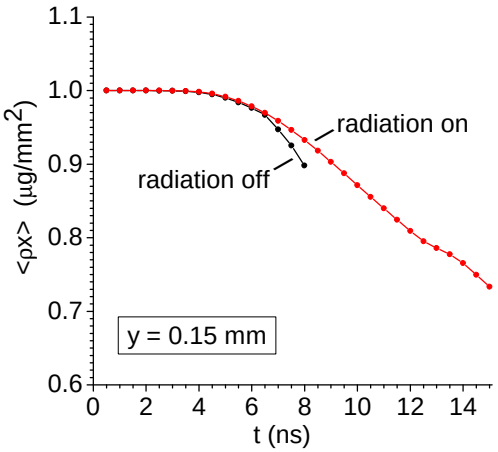

Figure 7: Evolution of the mass column density $\langle \rho x \rangle$ along the $y = 0.15$ mm line with and without thermal radiation.

radiation effects the depletion of $\langle \rho x \rangle$ sets in about 1 ns earlier because a larger fraction of the absorbed laser energy is transformed into the kinetic energy of expansion.

Figure 8 shows the profiles of the density and the ionization degree as functions of the mass coordinate $\langle \rho x \rangle$ across

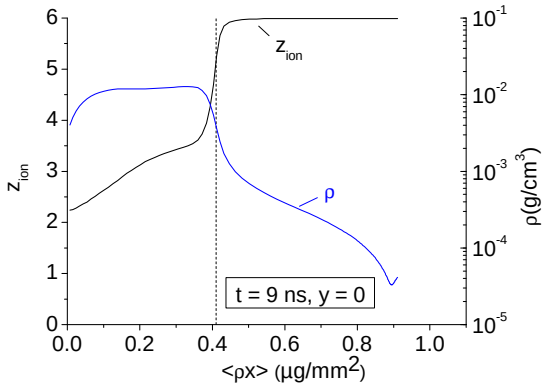

Figure 8: Profiles of the ionization degree (left ordinates) and the density (right ordinates) as functions of the longitudinal mass coordinate $\langle \rho x \rangle$ along the $y = 0$ line at $t = 9$ ns. The dashed vertical line marks the position of the critical surface.

the heated part of the foil at the latest suitable time $t = 9$ ns. As compared to the density profile for $t = 5$ ns in Fig. 6, now the peak density has dropped by another factor of $\simeq 5$ to $\rho \approx 0.01$ g/cm^3. The profile of the ionization degree is significantly non-homogeneous. Though about half of the foil mass has been fully ionized, the cold rear part still remains at a relatively low level of ionization $z_{ion} \approx 3$. Thus, even without examining the transverse non-uniformities we can conclude that the present combination of the target and laser-beam parameters produces a plasma configuration which is not quite suitable for clean ion-stopping experiments.

3.1.2. Modulated laser spot

Here we focus our attention on the transverse plasma non-uniformities caused by a strong modulation of the laser intensity across the focal spot. The intensity profile used in the simulations is given by Eq. 2 and plotted in Fig. 2b. For the case of 1ω light, the laser intensity varies over the focal spot by ±50% on the spatial scale of 100 μm. The 2D temperature distribution calculated with the modulated laser spot is presented in Fig. 9 for $t = 6$ and 10 ns (i.e. in the middle and at the end of the laser pulse). Figure 10 shows the analogous plot for the matter density at $t = 6$ ns.

Figures 9a and 10 clearly demonstrate how by $t = 4$–6 ns a non-uniformly irradiated foil breaks into clumps. The process of formation of dense and relatively cold clumps is similar to the hole-boring effect. In the hot areas that are subject to a stronger heating by the laser intensity peaks matter expands and the density drops significantly faster than in the colder parts irradiated by lower intensity. As a result of 2D matter redistribution between the hot and the cold areas, a strongly non-uniform transverse profile of the column density $\langle \rho x \rangle$ develops by the middle of the laser pulse. Figure 11 shows the transverse variation of $\langle \rho x \rangle$ along the y-coordinate at $t = 4.5$ ns, when the clumpy structure is most pronounced. It is seen that at this moment the spikes of $\langle \rho x \rangle$ are about a factor of 5 higher than the mean value. Accordingly, the narrow density spikes occupy a relatively small total fractional area of the assumed ion beam cross-section — an important factor for the ion stopping measurements.

However, as time goes on, the clumps get gradually dissipated, mainly by virtue of the energy transport by thermal radiation. As it is seen from Fig. 9b, by the end of the laser pulse the transverse temperature non-uniformity has all but vanished. The corresponding curve in Fig. 11 shows that by $t = 9$ ns the transverse variation of the column density $\langle \rho x \rangle$ across the laser focal spot drops to ±20%. At the same time, similar to the case of the uniform laser spot, the rear side of the foil still remains relatively cold, and the plasma slab is not fully ionized. The lateral rupture of the foil is even more pronounced than for the uniform spot. This is due to a steeper intensity gradient at the periphery of the focal spot.

To give a better feeling for the mechanism of clump dissipation, we have plotted in Fig. 12 the spectrum of the local radiation field at $t = 4.5$ ns in the cold center of the first clump ($y = 0.05$ mm), where the density and temperature at this moment are $\rho = 0.16$ g/cm^3, $T = 5.6$ eV. This spectrum was calculated by running a special simulation with 40 spectral groups equally spaced in $\log(h\nu)$ between 1 eV and 5 keV. This simulation demonstrated practically the same hydrodynamic behavior as the one with 5 spectral groups, having thus confirmed adequacy of our original spectral

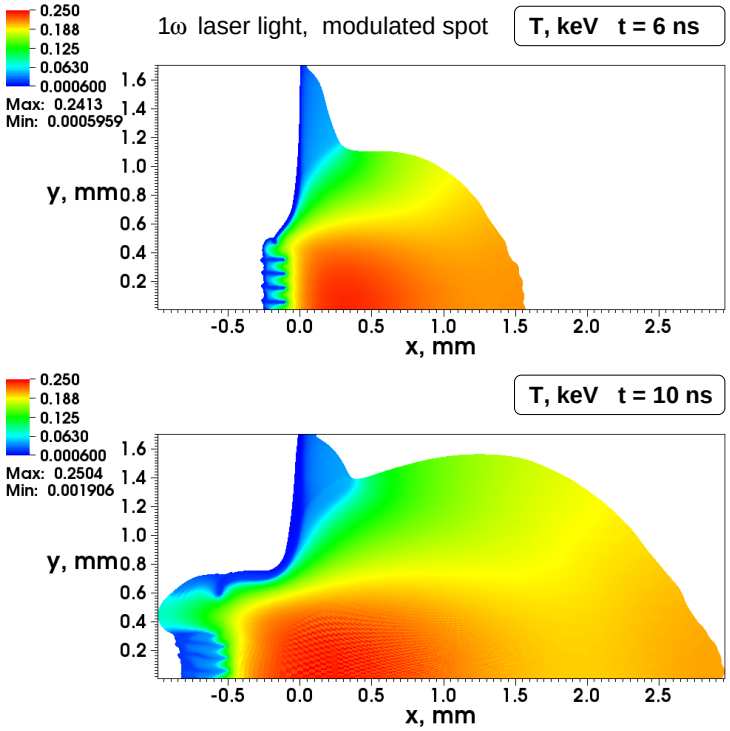

Figure 9: Two-dimensional color-contour plots of matter temperature for a modulated laser spot at 1ω for a) $t = 6$ and b) 10 ns.

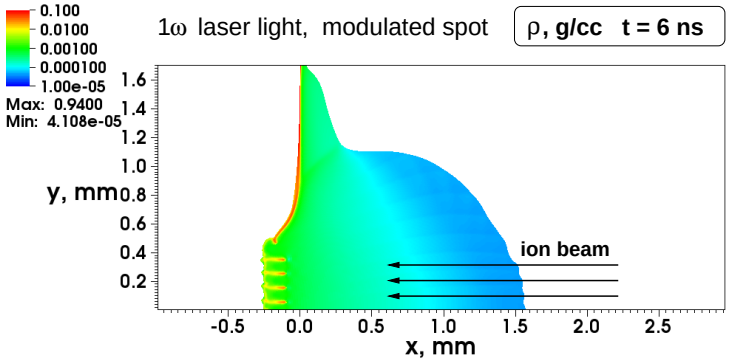

Figure 10: Two-dimensional color-contour plot of the density for a modulated laser spot at 1ω for $t = 6$ ns.

discretization (3). Plotted in Fig. 12 is the total radiation energy flux $U_i = \int_{\nu_i}^{\nu_{i+1}} d\nu \int_{4\pi} I_\nu(\Omega)\, d\Omega$ in each spectral group i, obtained by corresponding numerical integration of the spectral intensity $I_\nu(\Omega)$.

The spectrum in Fig. 12 reveals that by $t = 4.5$ ns the dense cold clumps are immersed into a radiation field with the intensity peaking at $h\nu \approx 0.3$–0.9 keV, i.e. around the carbon K-edge. The corresponding radiation flux by far exceeds the local Planckian intensity and originates as the recombination continuum and line emission from the electronic transitions to the K-shell of the hydrogen- and helium-like carbon ions. It is generated in a 3–5 μm thick transition layer around each clump, where the mean ionization degree of carbon ions — rising rapidly from its cold clump value of $z_{ion} \approx 1$ to the limit $z_{ion} = 6$ of full ionization in the hot ambient plasma — passes through the range of $3 \lesssim z_{ion} \lesssim 5.5$. This emission sheath is characterized by sharp gradients of temperature and density, and in our LTE model occurs at $T \approx 30$–70 eV.

Once the local radiation flux U_i is known, one can readily evaluate the radiative heating rate inside a cold clump

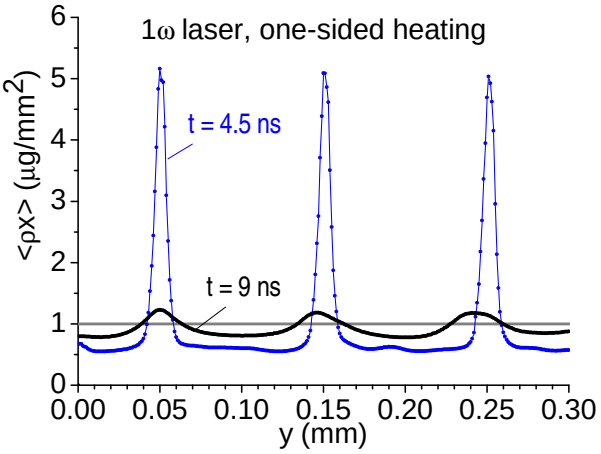

Figure 11: Transverse profile of the plasma column density $\langle \rho x \rangle$ for $t = 4.5$ and 9 ns.

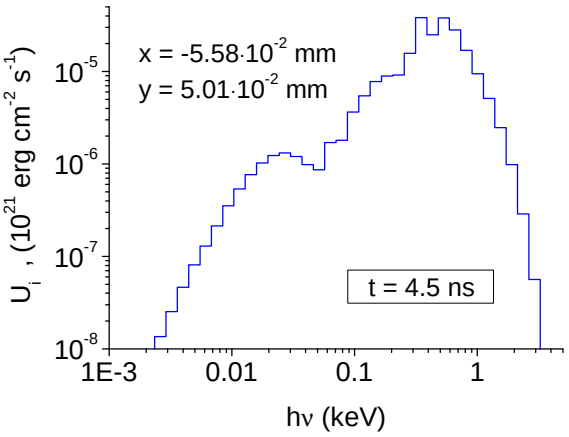

Figure 12: Spectrum of the local radiation field inside the first density clump at t=4.5 ns. Plotted is the 4π-integrated energy flux $U_i = \int_{\nu_i}^{\nu_{i+1}} d\nu \int_{4\pi} I_\nu(\Omega)\, d\Omega$ in each of the 40 spectral bins used in this particular simulation.

to be

$$Q = \sum_i U_i k_i \approx 6 \times 10^{20} \text{ erg cm}^{-3} \text{ s}^{-1}, \tag{4}$$

where k_i is the absorption coefficient in the i-th spectral bin (see Fig. 13). Then, by using a simple estimate $c_\text{v} \approx 6.3 \times 10^{11}$ erg g^{-1} eV^{-1} for the heat capacity of carbon, we find that the rate of temperature change in the center of a cold clump at $t = 4.5$ ns is

$$\frac{dT}{dt} \approx \frac{Q}{\rho c_\text{v}} \approx 6 \text{ eV ns}^{-1}, \tag{5}$$

implying temperature doubling roughly every nanosecond. This simple estimate illustrates how reabsorption of the radiation flux, generated in the emission sheath around dense clumps, disperses them on a timescale of 4–5 ns. As can be inferred from Fig. 13, the mean free path of photons in the relevant spectral range $h\nu \approx 0.3$–0.9 keV varies between 1 and 10 μm, i.e. the optical thickness of the cold clumps for penetrating radiation is roughly between 1 and 10, — which implies quite an efficient coupling of this radiation to the material inside the clumps.

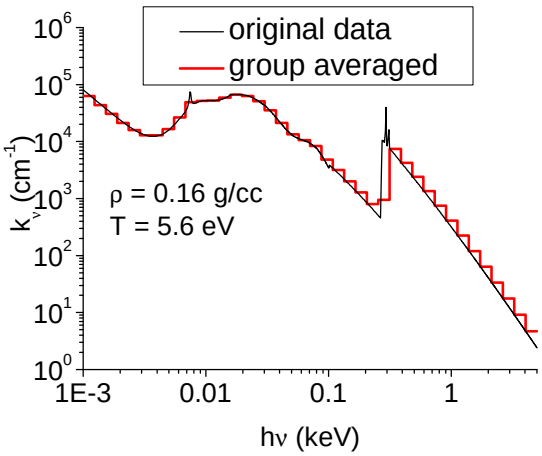

Figure 13: Radiation absorption coefficient k_ν [cm^{-1}] of carbon in a plasma with $\rho = 0.16$ g/cm^3, T=5.6 eV, characteristic for the interior of cold density clumps. Shown are the original data from the THERMOS code (thin curve) together with the group-averaged values for 40 spectral groups.

Our simulations demonstrate that the local radiation field is far from the Planckian equilibrium practically everywhere in the heated plasma — which brings the applicability of the LTE model into question. Unfortunately, we had no adequate non-LTE code at our disposal to make a direct comparison between the LTE and non-LTE results. However, the above analysis allows us to argue that the principal non-LTE effect in our situation should be simply a shift of the emission sheath (where $3 \lesssim z_{ion} \lesssim 5.5$) to somewhat different temperature and density values (i.e. by only a relatively short distance in space because of the sharp ρ and T gradients), while the overall mechanism of clump dissipation is not expected to undergo any significant changes.

It should be noted here that a laser accelerated thin foil can break into clumps not only because of spatial fluctuations of the laser intensity but also as a result of the RT instability at its non-linear stage — even when the laser irradiation is perfectly uniform. For a foil initially only 1 μm thick, the RT instability should develop from initial perturbations on a sub-micrometer scale. Because in the present simulation we had no such perturbations, we observed no effects from the RT instability. But even if we would have introduced these perturbations, the RT instability could hardly be expected to significantly affect our results on the transverse scale of 50–100 μm because this would require multiple non-linear cascading from the initial sub-micrometer modes, which can only occur after the accelerated foil travels several hundreds of micrometers. In addition, as was confirmed by a separate 2D run, the RT instability in our case is significantly suppressed by the radiative energy transport and does not pass into a well-developed non-linear stage for spatial scales above some 10 μm.

Apparently, a clumpy foil structure illustrated in Fig. 11 should somehow reveal itself in the experimental data on the ion stopping presented in [9]. In this experiment a beam of 4-MeV/u argon ions passed through the central area at $0 < y < r_b$, $r_b = 0.25$ mm. Clearly, the ions passing through the sharp peaks of column density $\langle \rho x \rangle$ should suffer a much higher energy loss than their neighbors penetrating the target at areas with reduced values of $\langle \rho x \rangle$. Since the areas with a depleted mass thickness occupy much larger fraction of the ion beam aperture, while the detection efficiency for the ions with a smaller energy loss is higher due to the energy dispersion of the ion imaging apparatus, the measured signal should be mainly composed of the ions penetrating the areas with a reduced column density. Hence, as the laser heated foil becomes clumpy, one would expect the recorded data on the ion stopping to be shifted towards the reduced values of the energy loss — and this is exactly what had been observed in the experiment reported in [9]. In full qualitative agreement with the above described picture, the measured ion energy loss, plotted as a function of time in Fig. 14, manifests a pronounced “dip” at about 4 ns after the laser was turned on.

The present interpretation was confirmed by simulations with a Monte-Carlo code for the charge transfer and energy loss of fast ions in the discussed experiment [9]. In these calculations it was assumed that only the ions passing through the areas of low column density contributed to the measured data. The plasma parameters were taken from the present 2D hydrodynamic simulation. Thus calculated values of the ion energy loss are represented in Fig. 14

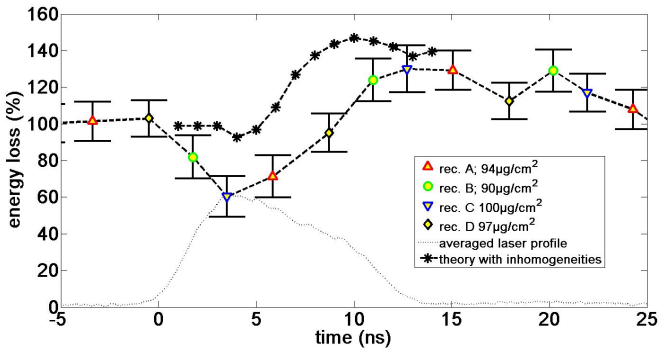

Figure 14: Experimental data and theoretical results for the energy loss of argon ions in the laser-produced carbon plasma. For $t < 0$ the ion beam passes through the cold foil; at $t = 0$ the laser is switched on. The average temporal profile of the laser pulse is shown at the bottom.

by a curve marked with black stars. Quantitatively, the agreement between theory and experiment is still far from perfect. However, there are no grounds to expect any better agreement before adequate 3D radiation-hydrodynamics simulations have been performed — which is beyond our present capabilities. As time goes on and the plasma homogenizes, the calculated energy loss values approach the experimental results and match them quite well for times $t \gtrsim 10$ ns.

As a next step, we could try to make our simulations more adequate for the discussed experiment by adapting the laser intensity profile more closely to the experimental conditions. Instead, we chose to address a more interesting question how the clumpy structure of the laser heated foil could be more efficiently suppressed in order to obtain a more uniform plasma layer suitable for the ion energy loss measurements before the effects of the global 2D expansion set in.

3.2. One-sided irradiation with the 2ω light

The calculations for a foil irradiated with the fundamental laser frequency have demonstrated that, if the intensity distribution in the laser spot is strongly modulated, the transverse non-uniformity of the created plasma layer significantly distorts the measured energy loss data. The situation can be improved if a doubled-frequency laser light is used. As in the case of the 1ω light, the calculations for 2ω were performed with both a uniform and a modulated laser spot. Figure 15 compares the longitudinal profiles of matter temperature T and mass-specific laser energy deposition rate q obtained in the 1ω and 2ω simulations with a uniform focal spot for $t = 5$ ns. One clearly sees that under the 2ω irradiation (i) the laser beam penetrates deeper into the foil, and (ii) the rear cold part of the foil is preheated by thermal x-rays to a higher temperature. Clearly, the enhanced heating of the cold and dense plasma regions facilitates faster dissipation of any type of dense clumps formed in the considered plasma volume.

More intense quasi-volumetric heating of the cold plasma regions is explained by higher efficiency of the energy conversion from the 2ω laser light into thermal x-rays of several hundreds eV. When the laser frequency is doubled, this leads to a four-fold increase of the critical plasma density $n_c = \pi mc^2/(e^2\lambda^2)$. The latter implies that in the vicinity of the critical surface, where most of the laser energy is absorbed, the x-ray emissivity will be enhanced by a significant factor. In particular, for the bremsstrahlung emission — which is the main radiation mechanism of a fully ionized plasma — the volumetric emissivity is $J \propto n_i n_e \propto \rho^2$, where n_e and n_i are the electron and the ion number densities [19]. As a result, the net x-ray energy losses by the end of the laser pulse approach 30%, i.e. almost double in comparison with the 1ω irradiation.

An important fact is that for the 2ω light the spatial scale of the laser intensity fluctuations becomes two times shorter than in 1ω, which also facilitates rapid leveling of the density non-uniformities. Figure 16 shows the transverse profiles of the longitudinal column density $\langle \rho x \rangle$ as calculated with $l = 50$ μm in Eq. (2) for the 2ω irradiation. The strongest variation of $\langle \rho x \rangle$ is now observed at $t = 3.5$ ns, where it amounts to about a factor 6 from peak to valley. However, by $t = 9$ ns the amplitude of these variations drops to ±4% — which is a factor of 5 less than by heating with the 1ω light. Note that, similar to the 1ω case, the longitudinal profile of the ionization degree still remains significantly nonuniform.

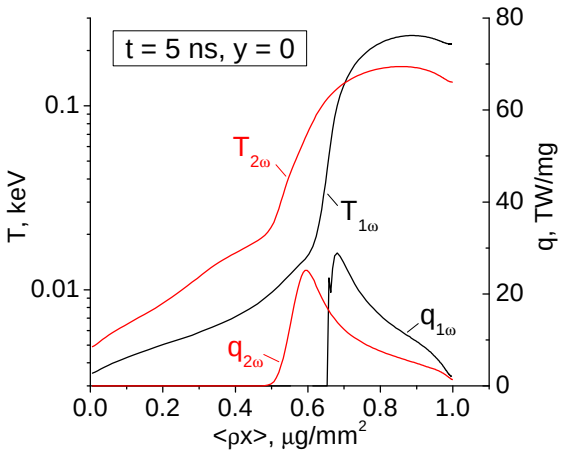

Figure 15: Longitudinal profiles of the mass-specific laser power deposition q and matter temperature T as functions of the mass thickness $\int \rho\, dx$ for the 1ω and 2ω laser irradiation with a uniform focal spot.

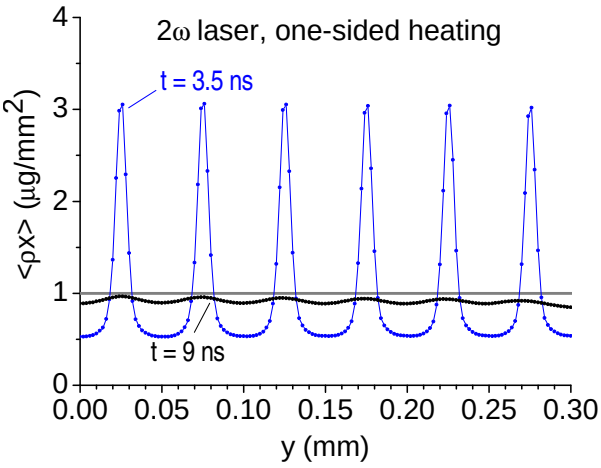

Figure 16: Transverse profiles of the plasma column density $\langle \rho x \rangle$ for the 2ω irradiation at $t = 3.5$ and 9 ns.

3.3. Two-sided irradiation with the 2ω light

The next logical step towards obtaining a uniform plasma layer would be to have the planar foil irradiated not just from one but from both its sides by two identical 2ω laser beams. Here we present the results of a simulation where two identical 2ω laser beams fall normally (along the x-axis) onto a carbon foil from two opposite directions. In this case the problem becomes fully symmetric with respect to the vertical $x = 0$ plane, and in the simulation it was sufficient to apply a reflective boundary condition along this plane. Note that now the cold part of the foil is no longer accelerated as a whole, which practically eliminates the eventual contribution of the Rayleigh-Taylor instability to the considered process of clump formation.

Because two opposite laser beams deposit two times more energy on the foil, one would expect the global 2D flow effects to appear earlier than in the one-sided case depicted in Fig. 7. The corresponding plot in Fig. 17 confirms this: under the two-sided irradiation the longitudinal column density $\langle \rho x \rangle$ at $y = 0.15$ mm drops by 10% from its initial value already at $t = 7.5$ ns, i.e. about 2 ns earlier than in the one-sided case. The non-monotonic decline of $\langle \rho x \rangle$, observed in Fig. 17 for the one-sided case at $t \approx 12 - 13$ ns, is explained by the temporal increase of the local column density due to the 2D plasma flow around the rim of the ruptured foil. The effect of foil rupture at the edge of the laser

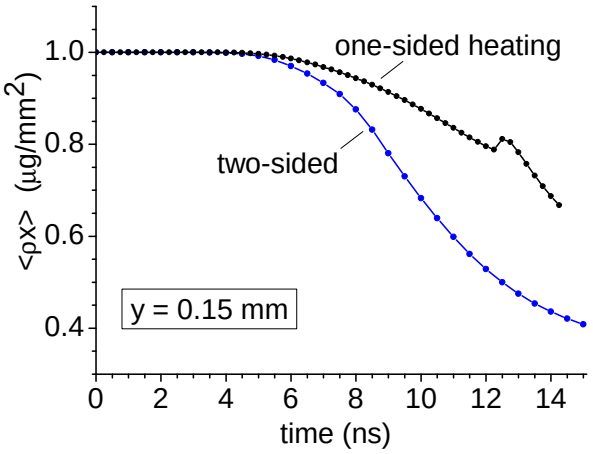

Figure 17: Temporal evolution of the column density $\langle \rho x \rangle$ along the $y = 0.15$ mm line for the one-sided and two-sided heating by the 2ω laser light with a uniform laser spot.

beam was discussed in the section 3.1.1.

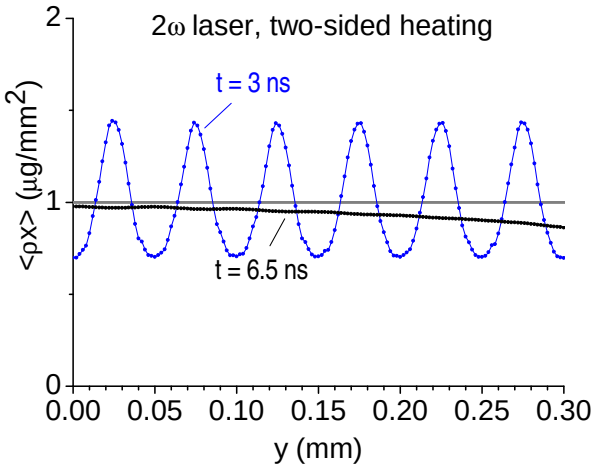

Figure 18: Transverse profiles of the plasma column density $\langle \rho x \rangle$ for the two-sided 2ω irradiation at $t = 3$ and 6.5 ns.

The impact of the strong spatial modulation (2) of the laser intensity with the period $l = 50\ \mu$m is demonstrated in Fig. 18: at $t = 3$ ns the induced modulation of the longitudinal plasma column density $\langle \rho x \rangle$ has the highest amplitude of roughly 2:1 — which is already significantly less than 6:1 in the case of the one-sided heating — and drops to a negligible value of ±0.5% by $t = 6.5$ ns. Figure 19 displays the longitudinal profiles of the ionization degree along the line $y = 0.125$ mm (a local minimum of the laser intensity) plotted for $t = 5$ and 6.5 ns. At $t = 5$ ns the cold central part of the foil still has an ionization degree of $z_{ion} \approx 4.5$, while by $t = 6.5$ ns the entire plasma column becomes fully ionized to $z_{ion} = 6$.

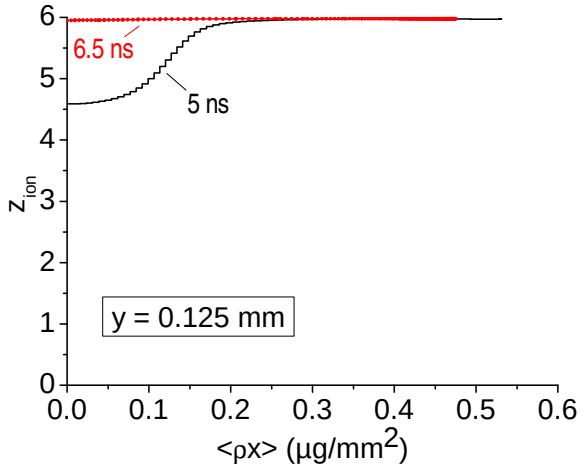

Figure 19: Longitudinal profiles of the ionization degree z_{ion} along the line $y = 0.125$ mm for the two-sided 2ω irradiation at $t = 5$ and 6.5 ns.

4. Conclusion

In this work, by using two-dimensional radiation hydrodynamics simulations, we have investigated how a uniform plasma layer, suitable for ion-stopping measurements, could be created by direct laser irradiation of a thin (sub-micrometer) carbon foil. The main parameters of the laser beam were taken from the ion stopping experiments performed recently with the nhelix laser at GSI [9]. A particular attention has been paid to suppression of the clumpy structure which develops in the created carbon plasma under the action of a strongly non-uniform intensity distribution across the laser focal spot.

As the main result of our study, we have shown that it is possible to find a suitable combination of the laser and target parameters for which a strongly non-uniform direct laser light produces a sufficiently uniform quasi one-dimensional plasma column that could be used to measure energy losses of fast ions in a plasma. It is found that the key role in smoothing out the evolving strong density and temperature fluctuations belongs to the energy transport by thermal radiation. Of course, the achieved quasi-uniform plasma state exists only within a certain limited time window.

In particular, we have demonstrated that the radiative dissipation of the density clumps in the heated foil can be significantly intensified by doubling the laser frequency. If, in addition, one adopts a scheme with the two-sided irradiation by two opposite laser beams, one ends up (after several nanoseconds) with (i) a virtual elimination of the longitudinal (with respect to the presumed trajectories of fast ions) non-uniformity of the degree of carbon plasma ionization, and (ii) the reduction of the transverse variations of the longitudinal column density $\langle \rho x \rangle$, induced by a 3:1 modulation of the focal laser intensity, to an insignificant level of $< 1\%$.

5. Acknowledgments

This work was supported by the Helmholtz Alliance Program of the Helmholtz Association, contract HA216/EMMI ”Extremes of Density and Temperature: Cosmic Matter in the Laboratory”, and by the Bundesministerium für Bildung und Forschung BMBF (Projects 06FY9085 and 06FY9080I).

References

[1] S. P. Ahlen, Rev. Mod. Phys. **52** (1980) 121.
[2] H. Geissel, H. Weick, C. Scheidenberger, R. Bimbot, D. Gardès, Nucl. Instr. and Meth. in Phys. Res. B **195** (2002) 3.
[3] I. Hofmann, G. Plass (Eds.), The HIDIF-Study, GSI-98-06 (1998).

[4] Max Tabak, James Hammer, Michael E. Glinsky, William L. Kruer, Scott C. Wilks, John Woodworth, E. Michael Campbell, Michael D. Perry, and Rodney J. Mason, Phys. Plasmas **1** (1994) 1626.
[5] M. Roth, T. E. Cowan, M. H. Key, S. P. Hatchett, C. Brown, W. Fountain, J. Johnson, D. M. Pennington, R. A. Snavely, S. C. Wilks, K. Yasuike, H. Ruhl, F. Pegoraro, S. V. Bulanov, E. M. Campbell, M. D. Perry, and H. Powell, Phys. Rev. Lett. **86** (2001) 436.
[6] C. Couillaud, R. Deicas, Ph. Nardin, M. A. Beuve, J. M. Guihaumé, M. Renaud, M. Cukier, C. Deutsch, and G. Maynard, Phys. Rev. E **49** (1994) 1545.
[7] M. Roth, C. Stöckl, W. Süß, O. Iwase, D. O. Gericke, R. Bock, D. H. H. Hoffmann, M. Geissel and W. Seelig, Europhys. Lett. **50** (2000) 28.
[8] M. Ogawa, Y. Oguri, U. Neuner, K. Nishigori, A. Sakumi, K. Shibata, J. Kobayashi, M. Kojima, M. Yoshida, J. Hasegawa, Nucl. Instr. and Meth. in Phys. Res. A **464** (2001) 72.
[9] A. Frank, A. Blažević, P. L. Grande, K. Harres, T. Heßling, D. H. H. Hoffmann, R. Knobloch-Maas, P. G. Kuznetsov, F. Nürnberg, A. Pelka, G. Schaumann, G. Schiwietz, A. Schökel, M. Schollmeier, D. Schumacher, J. Schütrumpf, V. V. Vatulin, O. A. Vinokurov, and M. Roth, Phys Rev E **81** (2010) 026401.
[10] G. Schaumann, M.S. Schollmeier, G. Rodriguez-Prieto, A. Blazevic, E. Brambrink, M. Geissel, S. Korostiy, P. Pirzadeh, M. Roth, F.B. Rosmej, A.Ya. Faenov, T.A. Pikuz, K. Tsigutkin, Y. Maron, N.A. Tahir, D.H.H. Hoffmann, Laser Part. Beams **23** (2005) 503
[11] V. Bagnoud, B. Aurand, A. Blazevic, S. Borneis, C. Bruske, B. Ecker, U. Eisenbarth, J. Fils, A. Frank, E. Gaul, S. Goette, C. Haefner, T. Hahn, K. Harres, H.-M. Heuck, D. Hochhaus, D. Hoffmann, D. Javorkova, H.-J. Kluge, T. Kuehl, S. Kunzer, M. Kreutz, T. Merz-Mantwill, P. Neumayer, E. Onkels, D. Reemts, O. Rosmej, M. Roth, T. Stoehlker, A. Tauschwitz, B. Zielbauer, D. Zimmer, and K. Witte, Appl. Phys. B **100** (2010) 137.
[12] M. M. Basko, J. Maruhn and An. Tauschwitz, GSI Scientific Report 2009: GSI Report 2010-1 (Darmstadt, Germany: Gesellschaft für Schwerionenforschung mbH) 2010, p. 410.
[13] M. M. Basko, P. V. Sasorov, M. Murakami, V. G. Novikov and A. S. Grushin, Plasma Phys. Control. Fusion **54** (2012) 055003; doi:10.1088/0741-3335/54/5/055003.
[14] Frank L. Addessio, John R. Baumgardner, John K. Dukowicz, Norman L. Johnson, Bryan A. Kashiwa, Rick M. Rauenzahn, Charles Zemach, CAVEAT: A Computer Code for Fluid Dynamics Problems With Large Distortion and Internal Slip LA-10613-MS-Rev. 1, UC-32 (Los Alamos: Los Alamos National Laboratory) 1992.
[15] M. M. Basko, J. Maruhn and An. Tauschwitz, J. Comput. Phys. **228** (2009) 2175.
[16] E. Livne and A. Glasner, J. Comput. Phys. **58** (1985) 59.
[17] M. M. Basko, High Temp. **23** (1985) 388.
[18] A.F. Nikiforov, V. G. Novikov and V. B. Uvarov, Quantum-Statistical Models of Hot Dense Matter: Methods for Computation of Opacity and Equation of State (Basel: Birkhauser), 2005.
[19] Ya. Zel'dovich, Yu. Raizer, Physics of Shock Waves and High-Temperature Hydrodynamic Phenomena (Dover Pubn Inc), 2002.